Optimized laser wakefield acceleration: Generating stable, high-energy, monoenergetic electron beams and demonstrating extreme-ultraviolet free-electron lasers

Zhan Jin,[1,3,*] Masaki Kando,[2,3,1,†] Yan-Jun Gu,[1,3] Kai Huang,[2,3] Nobuhiko Nakanii,[2,3] Izuru Daito,[2] Zhenzhe Lei,[1] Shingo Sato,[1] Hiroaki Sano,[1] Toshiya Muto,[1] Shigeru Yamamoto,[4,3] and Tomonao Hosokai[1,3]

[1]*SANKEN, The University of Osaka, Mihogaoka 8-1, Ibaraki, Osaka 567-0047, Japan*

[2]*Kansai Institute for Photon Science (KPSI), National Institutes for Quantum Science and Technology (QST), 8-1-7 Umemidai, Kizugawa, Kyoto 619-0215, Japan*

[3]*Laser Accelerator R&D, Innovative Light Sources Division, RIKEN SPring-8 Center, Kouto 1-1-1, Sayo-cho, Sayo-gun, Hyogo 679-5148, Japan*

[4]*Photon Factory, Institute of Materials Structure Science, High Energy Accelerator Research Organization, KEK, 1-1 Oho, Tsukuba, Ibaraki 305-0801, Japan*

(Received 23 July 2025; accepted 6 January 2026; published 24 February 2026)

Free electron lasers (FELs) are powerful, tunable light sources capable of delivering ultrashort, coherent radiation over a wide spectral range, but their broad scientific and technological impact is limited by the size and cost of large-scale accelerators. Laser wakefield acceleration (LWFA) offers a compact alternative via the ultrahigh accelerating gradients, though achieving FEL gain with such beams remains a major challenge due to the stringent beam-quality requirements. Here, we present a successful demonstration of a laser-plasma accelerator-driven FEL operating at a central wavelength of 40 nm with a highly nonlinear gain. A compact 0.8 J laser system, combined with precise control over the plasma-density profile, injection conditions, and the stability of both laser wave front and gas jet, enabled the generation of high-quality monoenergetic electron beams with excellent shot-to-shot reproducibility. A comprehensive start-to-end simulation framework was established, incorporating beam acceleration, transport, and FEL generation. Each stage of the simulation shows good agreement with the experimental diagnostics. The resulting FEL radiation exhibits clear exponential gain of approximately 20 times. This work highlights a reliable route toward compact, tunable, x-ray FELs driven by LWFA, and represents a significant step toward practical applications of laser-plasma-based light sources.

DOI: 10.1103/qvg7-ng8n

I. INTRODUCTION

The pursuit of high-energy particle accelerators has long been a cornerstone of experimental physics, providing profound insights into the fundamental nature of matter and the universe. Accelerators, such as radiofrequency (RF) linear accelerators and synchrotrons, have achieved remarkable successes but are inherently limited by their size, cost, and the maximum achievable accelerating gradients. To address these limitations, the concept of laser wakefield acceleration (LWFA) has emerged as a revolutionary technique, promising compact and cost-effective alternatives capable of delivering ultrahigh acceleration gradients [1–6].

Laser wakefield acceleration relies on the interaction between an ultraintense laser pulse and a plasma medium to generate wakefields with electric fields exceeding 100 GV/m. This process, first proposed by Tajima and Dawson in 1979 [1], involves a high-power laser pulse [2] (typically terawatt to petawatt range) focused into a plasma, driving electrons out of its path and creating a trailing plasma wave. Electrons injected into the proper phase of this wakefield can be accelerated to relativistic speeds over millimeter-scale distances, enabling the production of high-energy electron beams in a compact setup.

Recent experimental achievements have demonstrated the potential of LWFA to produce high-quality electron beams with energy in the multi-GeV range [3–5]. Stable 24-h operation of LWFA has also been demonstrated, which makes statistical studies like data mining and machine learning possible [6].

Integrating LWFA with free electron lasers (FELs) represents a significant advancement in light-source technology [7–11]. FELs generate coherent, high-brightness x-rays by passing relativistic electron beams through a periodic magnetic structure known as an undulator. The combination of LWFA and FELs promises compact, ultrashort, high-intensity x-ray sources that are more accessible and cost effective. However, the shot-to-shot variation in the LWFA electron-beam parameters remains still significant compared to RF accelerators, which increases the difficulty of successful electron-beam transportation and undulator amplification.

*Contact author: jin@sanken.osaka-u.ac.jp
†Contact author: kando.masaki@qst.go.jp

Published by the American Physical Society under the terms of the Creative Commons Attribution 4.0 International license. Further distribution of this work must maintain attribution to the author(s) and the published article's title, journal citation, and DOI.

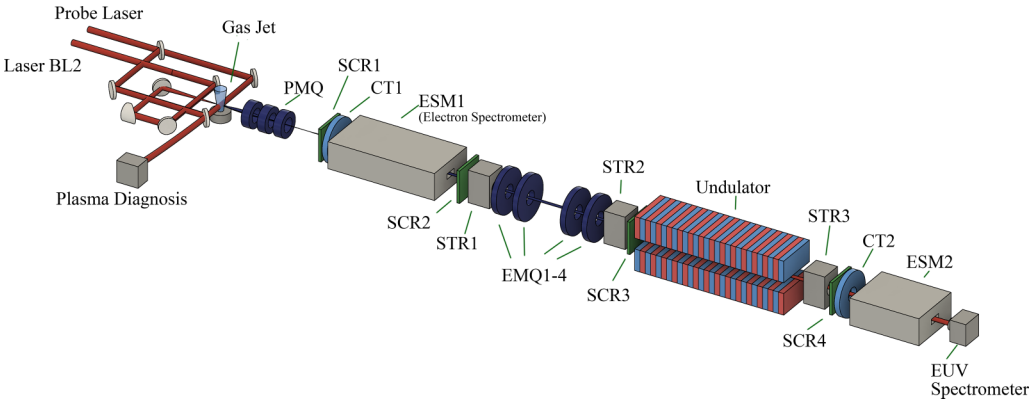


FIG. 1. Schematic experimental setup. Detailed descriptions are provided in the main text.

Here, we report comprehensive studies to improve the LWFA beam quality and stability for FEL generation. By ensuring precise injection control, stabilization of the laser wave front, and optimal performance of the gas jet, as well as by optimizing phase rotation and beam loading, we can generate monoenergetic electron beams with an energy spread of less than 1%, energies approaching 400 MeV, pointing stability of less than 0.5 mrad, and energy stability of less than 6%. Demonstration experiments by sending these beams into an undulator have shown a FEL gain of 20 times in XUV range.

II. EXPERIMENTAL SETUP

The experiment was conducted at laser acceleration platform LAPLACIAN (Laser Acceleration Platform as a Coordinated Innovative Anchor), a specialized facility designed for laser wakefield acceleration research (Fig. 1). This platform is located at the RIKEN SPring-8 Center. The laser system utilized in the platform is a custom-built Ti:Sapphire femtosecond laser system (amplitude laser) capable of delivering three laser beams (beamline 1, 2, and 3) with adjustable parameters, all synchronized with each other.

For the FEL experiment, beamline 2 was used as the driver laser, providing a laser pulse energy of 0.8 J and a minimum pulse duration of 21 fs after compression. The laser contrast was measured to be 10^{-11} at 50 ps before the main pulse. The Strehl ratio was approximately 0.95 after the final amplifier. A gold-coated off-axis parabola with a focal length of 1500 mm was used to focus the laser onto the gas target.

Beamline 1, with a similar pulse duration, served as a probe laser for diagnostics, including interferometry, schlieren imaging, and electro-optic measurements for electron bunch length. The spatial distribution of the electron beams was measured using a movable phosphor screen (SCR 1) (Mitsubishi Chemical Co. Ltd., DRZ-High) located 1 m from the electron source. The electron energy was measured with a movable electron spectrometer (ESM 1) with a magnetic field of 0.55 T, a length of 900 mm, and a maximum measurable energy of approximately 2 GeV. The ESM was situated 2.5 m from the electron source, and the same type of phosphor screen (DRZ-High) was also used in ESM 1. Charged-coupled device cameras (Princeton Instruments, ProEM-HS: 1024BX3) with an image intensifier were employed to record the scintillating images.

III. INJECTION CONTROL

Precise control of electron injection is a critical factor for achieving a stable LWFA system. Self-injection [12], or self-wave-breaking, typically occurs at high plasma densities and high laser intensities where the plasma wave enters a strongly nonlinear regime. Due to imperfect laser and plasma conditions, this wave breaking is often initiated by the growth of instabilities, leading to poor repeatability and stability in electron injection.

To effectively control injections, several schemes have been developed, including ionization injection [13,14], optical injection (colliding pulse injection) [15], density down-ramp injection (shock injection) [16], and hybrids of these methods [17]. For applications such as FEL generation, an electron beam with low energy spread, low emittance, and high peak current is required. This necessitates controlling the injection within a localized spatial and temporal region. A shorter injection window ensures consistency in the initial conditions of injected electrons, which is critical for reducing the energy spread. Therefore, shock injection is a promising candidate, as it injects electrons into the plasma wake only within a thin density down-ramp region.

In our experiments, a supersonic nozzle was used to generate a hydrogen gas jet in a vacuum chamber, as shown in Fig. 2(a). An obstacle (knife edge) was positioned 3 mm above the nozzle exit. When the gas hits the knife edge, it becomes compressed and forms a shock wave. The driver laser axis was located 1 mm above the knife edge. The minimum thickness of the shock wave is influenced by the molecular mean-free path (μm in our case). The plasma-density distribution [Fig. 2(b)], measured using a Mach-Zehnder interferometer (see Appendix for details), shows that the thickness of the shock down-ramp region is less than 20 μm. It shall be noted that this value can be overestimated due to the resolution limit of the imaging system, and also the transverse size of the target (the plasma channel has a diameter of about 100 μm).

When the wakefield encounters such a sharp density down-ramp, the plasma wavelength increases, causing the phase velocity of the wake to decrease. Consequently, the

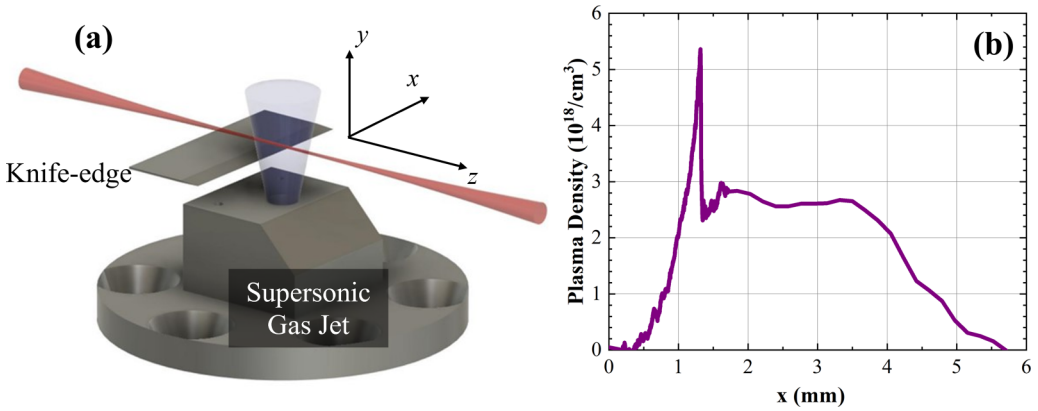


FIG. 2. (a) Sketch of shock injection target setup. (b) Plasma-density distribution along laser axis, measured with a Mach-Zehnder interferometer.

wave breaking condition is satisfied, allowing electrons to be injected into the bubble. The plasma-density plateau following the shock ensures constant acceleration without further injection.

A stable laser wakefield accelerator relies on two key factors: a well-tailored, stable plasma (gas)-density distribution and a stable drive laser with suitable parameters. Efforts have been made to enhance both plasma and laser stability.

IV. STABILIZATION OF LASER WAVE FRONT

The instability of the laser system can be attributed to various parameters, including energy, pointing, pulse duration, and contrast. Recent studies indicate that the laser wave front may be the dominant factor [17,18]. Improving laser wave front stability may require numerous modifications to the entire laser system, such as stabilizing the pump lasers, controlling vibrations, and reducing heat sources that cause air flow along the optical path. These modifications are both time- and cost-intensive.

An easier approach to enhance laser wave front stability involves simply adding a circular mask whose inner diameter is smaller than the laser beam size. Our measurements show that the outer part of the laser beam exhibits worse wave front stability than the inner circle. This may be due to the outer region's increased sensitivity to thermal lensing stability caused by fluctuations in the pump laser energy on the amplifier's crystal. Further measurements are needed to verify this speculation.

Therefore, a mask was installed before the parabola mirror in our system. As shown in Figs. 3(a)–3(c), without the mask, the root-mean-square (RMS) wave front phase of the entire beam (approximately 70 mm in diameter) was about 0.1256λ (s.d. 0.0082λ). With a 60-mm-diameter mask installed, the remaining laser had an RMS wave front phase of about 0.0571λ (s.d. 0.0046λ). The Strehl ratio has also improved from 0.81 (s.d. 0.03) to 0.88 (s.d. 0.017). The defocus of the laser shows similar values with and without the mask, while the standard deviation was reduced from 0.014 to 0.008. The results indicate an approximate 50% reduction in wave front instability with the mask. However, about 20% of the laser energy is sacrificed (reduced from 800 to 600 mJ).

The electron pointing stability was measured using SCR 1 to evaluate the effect of the mask. Under identical target configurations, the electron-beam pointing stability improved significantly from 10 mrad (without the mask) to 1.3 mrad (with the mask), as shown in Figs. 3(d) and 3(e). However, due to the laser energy loss caused by the mask, the peak electron-beam energy decreased from approximately 600 to 400 MeV, as measured with the ESM.

In addition, the mask provides a straightforward method for fine-tuning the electron-beam direction [19]. Given that the energy stability of LWFA beams is still inferior to that of RF accelerators, an electron source aligned with the beamline axis is crucial for effective beam transport. This alignment accuracy increases the likelihood of successful beam delivery and suppresses unnecessary emittance growth.

One approach to control beam direction involves adjusting the angular chirp of the drive laser [20]. However, this method requires precise tuning of the angles of gratings and mirrors within the pulse compressor, which can also alter the laser pulse duration. In contrast, moving the transverse position of the mask offers a simple and effective way to precisely control the LWFA electron-beam direction without requiring additional adjustments to the optics in the laser system or the gas target.

V. STABILIZATION OF PLASMA-DENSITY DISTRIBUTION

Due to imperfections in the gas feed line, turbulence is likely to form, leading to unpredictable gas velocity and density distributions at the nozzle exit. To address this issue, a systematic study was conducted [21–23]. Both computational fluid dynamics (CFD) simulations and experimental measurements revealed that the stilling chamber of a gas nozzle with sufficient length, longer than the characteristic turbulence length, can effectively suppress fluid instabilities.

A comparison between a conical nozzle with and without a stilling chamber demonstrated that gas-density stability improved by a factor of 4, while shock position stability improved by nearly an order of magnitude. Consequently,

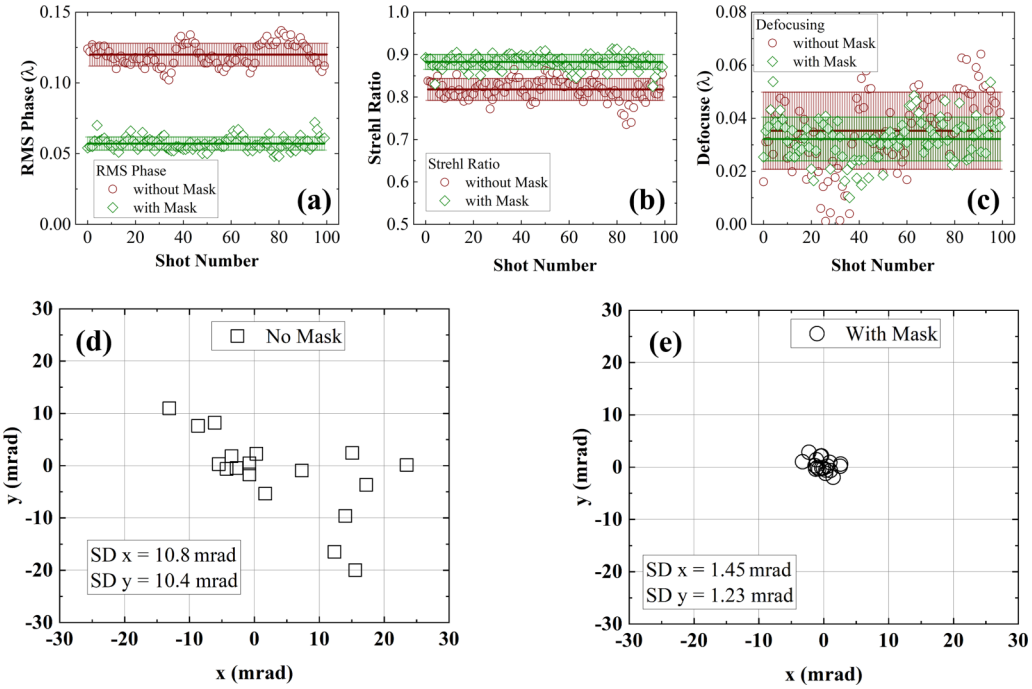


FIG. 3. Effect of the mask on the laser wave front and electron-beam pointing. (a)–(c) The measured wave front RMS phase, Strehl ratio, defocusing, respectively. (d), (e) Electron pointing stability with and without the mask.

the measured electron pointing stability also improved with the increasing of stilling chamber length (Fig. 4). Notably, when the stilling chamber length was increased from 15 to 20 mm, shock position stability improved, indicating better fluid stability. However, the electron pointing stability showed no further enhancement. These results suggest that the primary contribution to electron instability may be attributed to fluctuations in the laser after the gas target has reached saturation stability.

VI. BEAM LOADING

The beam-loading effect plays a crucial role in determining the electron parameters after acceleration. Comprehensive studies [17,18] have shown that overinjection leads to reduced energy gain and a broader energy spread. In contrast, precise control of the injected charge can "flatten" the wakefield along the injected beam bunch, resulting in a more monoenergetic beam spectrum [24].

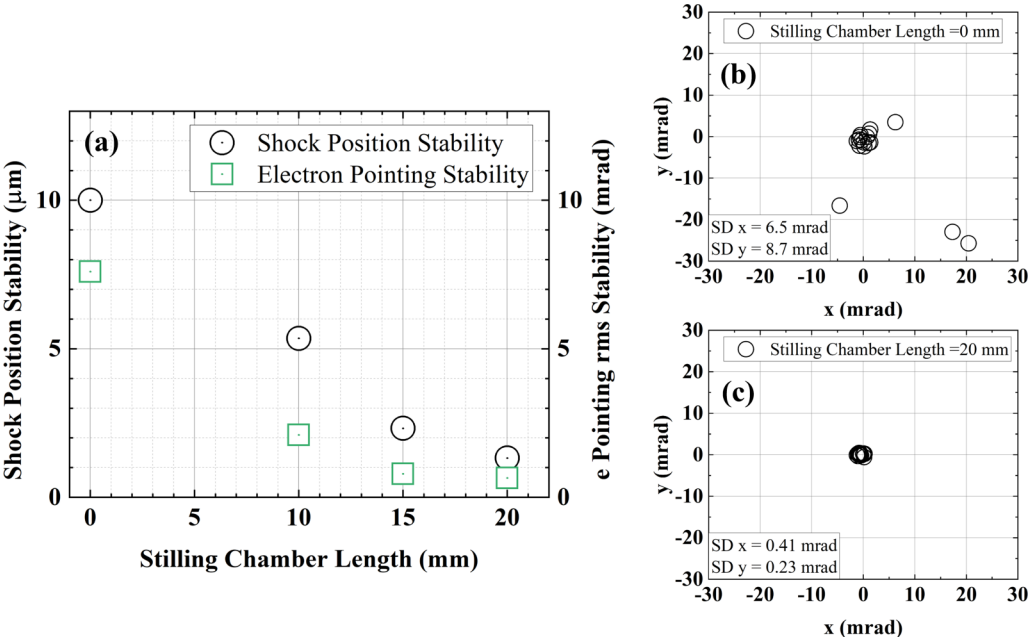


FIG. 4. (a) Electron beam's pointing stability improves with longer stilling chamber. Panels (b) and (c) compare the measured beam pointing without stilling chamber and with 20-mm-length stilling chamber.

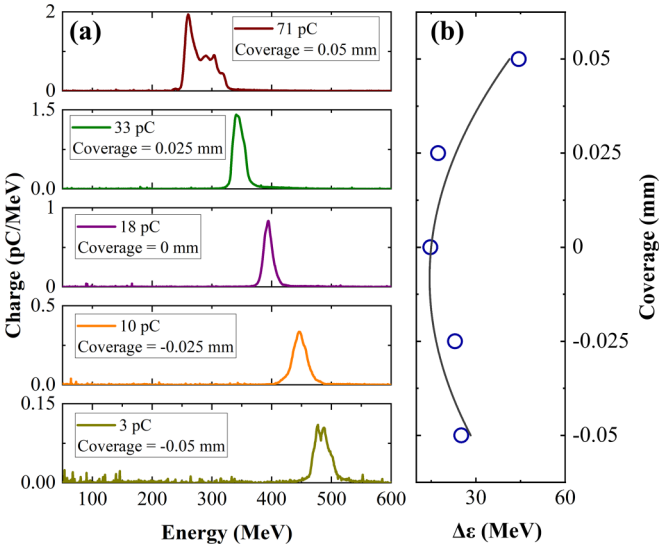


FIG. 5. Measured electron spectrum with different coverage values. Lower injection charge results in higher energy gain. However, the energy spread shows a minimum value with charge around 20 pC.

The injected charge in the shock injection scheme is typically determined by (1) the plasma densities at the shock peak and the plateau region, i.e., the shock intensity, (2) the shock thickness, and (3) the laser intensity during the density transition. In our experiments, the injection charge is controlled by adjusting the parameter "coverage," defined as the relative position between the blade and the nozzle along the laser propagation direction ($z_{\text{blade}} - z_{\text{nozzle}}$) [16]. It should be noted that the blade is positioned at the front edge of the supersonic gas jet. Increasing the coverage enhances the shock intensity, thereby resulting in higher-charge injection.

Figure 5 illustrates the typical charge loading effect observed when varying the coverage. The results are well consistent with those reported in Ref. [18]. It was found that an injection charge exceeding 30 pC results in oveinjection under our experimental conditions. Further detailed discussions are provided in the next section.

VII. PHASE ROTATION

The (z, ε) phase rotation in the wakefield plays a critical role in determining the final electron-beam quality. This phenomenon was examined in detail through quasicylindrical particle-in-cell (PIC) simulations using the relativistic electromagnetic code FBPIC [25]. The density profile in the simulation was based on the CFD results, which is well consistent with the experimental measurements, as shown in Fig. 2(b). A linearly polarized laser pulse with a peak intensity of $I = 7 \times 10^{18}\,\text{W/cm}^2$ was focused 1 mm behind the density shock. Both the temporal and transverse spatial profiles were modeled with Gaussian distributions, having a pulse duration of $\tau = 22\,\text{fs}$ and a beam waist of $w = 18\,\mu\text{m}$.

The initial stage of phase deformation is phase expansion. After the electron bunch is injected at the density shock, it resides at the rear of the wakefield, where electrons at the front of the bunch experience a stronger electric field. This results in the expansion of the (z, ε) phase space until the electrons at the tail encounter the same field strength as those at the front. Assuming the initial momentum of the injected electrons is negligible, the phase expansion leads to a maximum energy deviation given by $\Delta\varepsilon = eE_{\text{wb}}\frac{c\sigma_e}{v_e - v_{\text{ph}}}$, where $E_{\text{wb}} = \frac{m_e c\omega_{\text{pe}}}{e}$ is the maximum wakefield strength, σ_e is the electron bunch length, v_e is the electron velocity, and v_{ph} is the wakefield phase velocity. The term $\frac{c\sigma_e}{v_e - v_{\text{ph}}}$ represents the distance in the laboratory frame corresponding to the relative shift of σ_e in the wakefield frame. The electron-density distribution during the phase-expansion stage is shown in Fig. 6(a), where the red line represents the longitudinal electric field. At this point, the field strength at the tail of the bunch is weaker than that at the head, indicating the phase expansion. The corresponding energy spectrum is depicted by the blue line, which refers to the left y axis in Fig. 6. The (z, ε) projection is presented as a green scatter plot.

The second stage is phase compression, which corresponds to the phase rotation described in Refs. [26,27], where the slope of the (z, ε) phase space becomes less steep. At this stage, the tail electrons experience a higher acceleration gradient, resulting in the compression of the phase space. A typical phase compression state is shown in Fig. 6(b), approximately 1 mm after injection. The energy deviation of the electrons is reduced. To achieve a monoenergetic beam, the slope of (z, ε) must become flat. The phase compression effect in the linear wakefield case can be approximated as $d\varepsilon/dz = ek_{\text{wb}}\sigma_e$, where $k_{\text{wb}} = E_{\text{wb}}/(\lambda_p/2)$ represents the wakefield gradient. The compression process concludes when the electrons at the tail attain an energy similar to the rest of the bunch.

According to this model, the total length encompassing both the phase expansion and compression stages is approximately 2.23 mm. This prediction agrees with the simulation results shown in Fig. 6(c), which demonstrate a monoenergetic beam with a peak energy of approximately 190 MeV and a flat (z, ε) phase space.

Figure 6(c) also reveals that the tail electrons remain under acceleration, experiencing a stronger field compared to the head. This suggests that the (z, ε) phase space will undergo over-rotation with further propagation in the wakefield, leading to an increase in energy spread. A typical over-rotation scenario is depicted in Fig. 6(d), corresponding to the high-energy tail observed in experimentally detuned cases.

The model suggests that, in the linear wakefield regime, there exists an optimal acceleration length for a given plasma density to produce a monoenergetic electron beam. Insufficient acceleration distances result in a low-energy tail in the spectrum, while excessive distances lead to a high-energy tail. In a nonlinear plasma-wave regime, the phase expansion stage will be shortened, resulting in a reduction of the monoenergetic peak. It is also important to note that the above analysis does not account for the beam-loading effect. If the injected electron beam contains sufficient charge, the Coulomb field modifies the wakefield, leading to a more flattened configuration [24]. Consequently, the term k_{wb} is no longer constant, effectively extending the optimal acceleration length. This explains why high-charge beams exhibit higher peak energy at the monoenergetic condition, as observed in the experiments, as shown in Figs. 9(c) and 9(d).

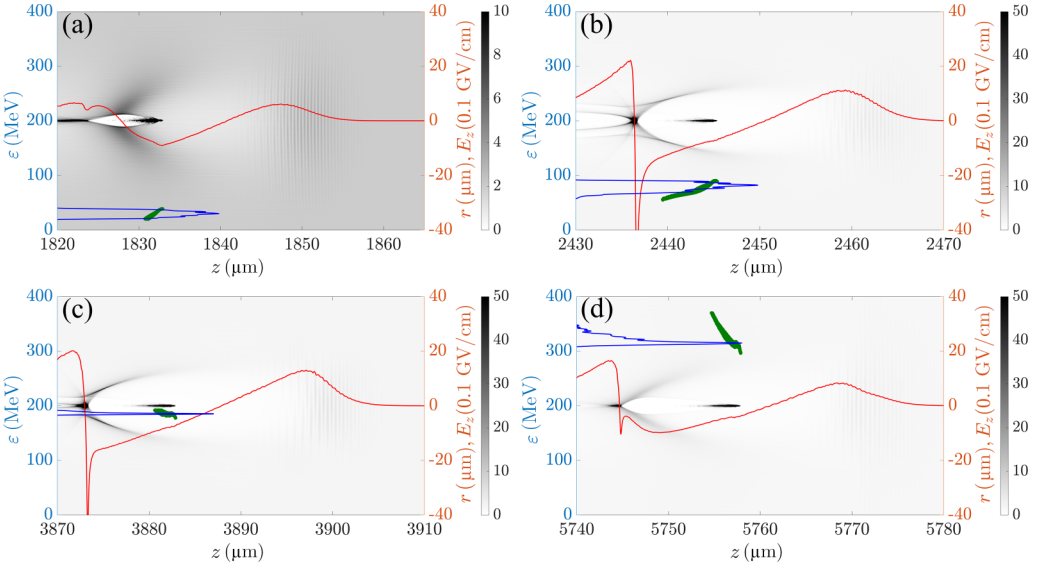


FIG. 6. PIC simulation of phase-rotation process with low injection charge. Panel (a) gives the (z, ε) phase when electron bunch is under the phase expansion stage. The (z, ε) phase space before, at, and after the dechirping is shown in panels (b)–(d), respectively.

The phase-rotation effect on the electron spectrum can be experimentally verified by varying the relative distance between the shock position (z_{shock}) and the longitudinal laser-focus position (z_{focus}). This relative distance influences the laser self-focusing behavior within the plasma, thereby affecting the effective acceleration gain. It should be noted that altering z_{focus}-z_{shock} also impacts the injection charge, as stronger laser intensity at the shock results in a higher injected charge [28,29]. However, this effect can be balanced by fine-tuning the coverage, i.e., adjusting the shock intensity. With an appropriately controlled injection charge, the phase-rotation effect can be clearly observed as a transition in the spectrum shape (Fig. 7): from low peak energy with a low-energy tail, to a monoenergetic spectrum with moderate central energy, and finally to high peak energy with a high-energy tail.

The combination of phase rotation and charge loading can be utilized to fine-tune the energy spread of the electron beam. As shown in Fig. 5, an injection charge of less than 10 pC results in higher energy gain but a broader energy spread, indicative of an over-phase-rotation condition. Conversely, with an injection charge of approximately 20 pC, the measured spectrum exhibits the narrowest energy spread. These results suggest that optimal beam loading can effectively flatten the acceleration field, leading to a final dechirped output spectrum. This highlights the importance of precise control over the injection charge to achieve desirable beam characteristics.

Full-parameter optimization is particularly challenging in our system due to its low repetition rate, which is limited by vacuum constraints and potential damage issues. Bayesian or genetic optimization algorithms [30] would substantially improve the efficiency of such parameter scans. In the present experiment, the gas pressure and the distance between the laser axis and the gas-jet exit were fixed to maintain a plasma density of $(2–3) \times 10^{18}\,\text{cm}^{-3}$. The relative position between the laser focus and the shock front affects both the injected charge and the phase rotation. We therefore set the (vacuum) laser-focus position within a range of 0–1 mm downstream of the shock. Outside this range, the electron-beam stability deteriorated, likely because the laser focal profile becomes unstable beyond the Rayleigh length.

The most critical parameter in our fine-tuning procedure is the blade insertion, i.e., the coverage. As shown in Fig. 5, variations of only a few tens of micrometers in the coverage significantly affect the injected charge. Under our experimental conditions, the acceleration length is sufficiently long that, in the absence of beam loading, the beam would undergo excessive phase rotation. To control the final energy spread, we therefore scanned the coverage in micrometer-scale steps to precisely adjust the injected charge and, consequently, the beam-loading effect.

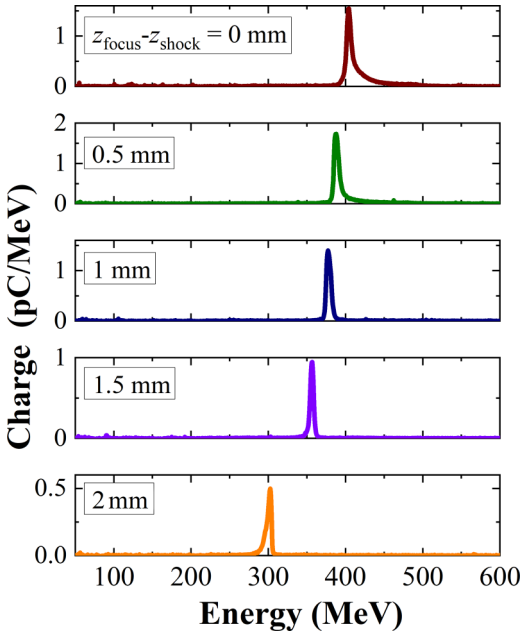


FIG. 7. Experimental demonstration of phase-rotation effect by varying the relative distance between the shock position (z_{shock}) and the longitudinal laser-focus position (z_{focus}).

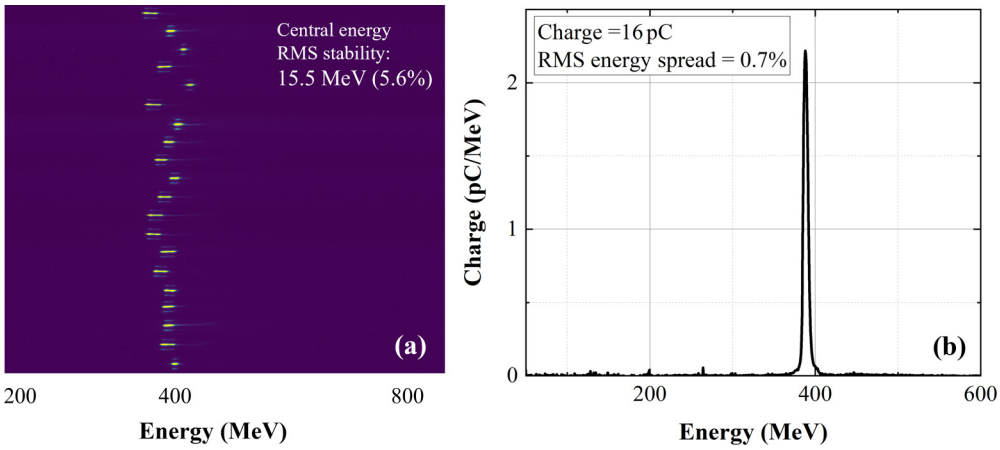


FIG. 8. Measured electron spectrum after optimization.

Figure 8(a) presents electron spectrum data from 20 consecutive shots after optimization. A clear beam-loading effect, similar to that shown in Fig. 5, is still observable under the "same" parameters. This suggests that the drive laser remains insufficiently stable. The average central energy was approximately 390 MeV, with a standard deviation of 5.6%, and the mean charge was 25 pC, with a standard deviation of 29%. The mean energy spread was measured to be 1.5%, with a standard deviation of 33%. An optimal spectrum is shown in Fig. 8(b), featuring an energy spread of 0.7%. It should be noted that the measured energy spread is likely overestimated owing to the resolution limitations of our electron spectrometer (ESM 1). Deconvolution, accounting for the resolution of ESM 1, indicates a reconstructed minimum energy spread of approximately 0.2% (see Appendix 2 for more detail).However, additional measurements employing a higher-resolution spectrometer will be required to confirm this result.

VIII. START-TO-END SIMULATION

Here, we employ several numerical codes to conduct start-to-end simulation, demonstrating electron generation in a gas jet, beam transport in the beamline, and free electron lasing in the undulator.

Electron generation was conducted using FBPIC code [25], which calculates a cylindrical grid for the fields, as the full 3D information of electrons is essential for beam transport and FEL simulations. For physical situations that have close-to-cylindrical symmetry, it is more efficient compared to the simulation on a 3D Cartesian grid. The simulation used a moving window of 75 μm (longitudinal direction, z) and 80 μm (radial direction, r) having grid points of 3000 and 1200, respectively. The azimuthal degree was 2 and the time step was 0.083 fs. The particle numbers per cell were 2 in z and r directions and 4 in the azimuthal direction. The normalized laser amplitude was $a_0 = 1.8$, the pulse duration was 22 fs, and the spot size was $w_0 = 20$ μm. Figure 9 shows a typical result that well reproduces the measured electron-beam qualities.

It can be observed that the slope of the (z, ε) phase space already exhibits signs of over-rotation. However, flattening occurs in regions of high charge density, resulting in a narrow energy spread of approximately 0.8%. This emphasizes the critical importance of carefully balancing phase rotation and beam loading, as discussed in the previous section.

The peak energy in the simulation was about 390 MeV, which is well consistent with the experimental results. The corresponding normalized transverse emittance were 0.1 and 0.06 mm mrad, respectively.

Then, the generated electron was transported by the beamline using the GPT code (General Particle Tracer) [31]. The space-charge 3D model was employed for the space-charge calculation, which calculates the field from relativistic particle-particle interaction. Because of the high electron energy and low charge, the space-charge effect did not affect the beam transport calculations significantly.

Finally, the undulator radiation was calculated with SIMPLEX 3.1, a FEL simulation code [32,33]. The details of GPT and SIMPLEX simulation results will be mentioned in the following sections to compare with the corresponding experimental measurements.

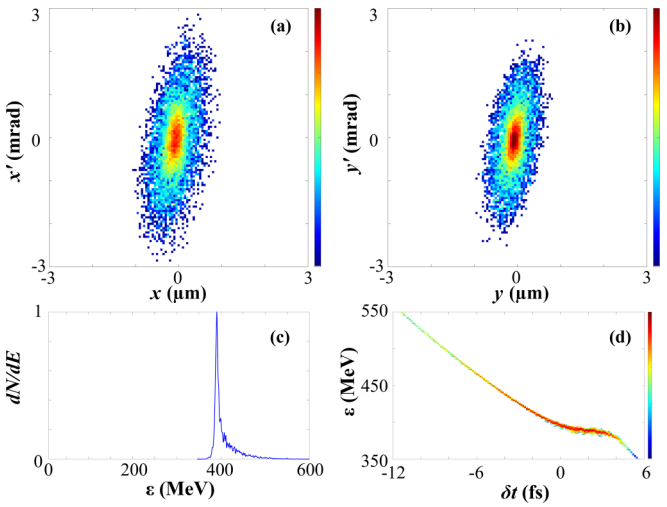


FIG. 9. Electron-beam parameters from PIC simulation. Panels (a) and (b) show the electron distribution in position-momentum phase space. Panel (c) presents the energy spectrum, while panel (d) illustrates the phase rotation.

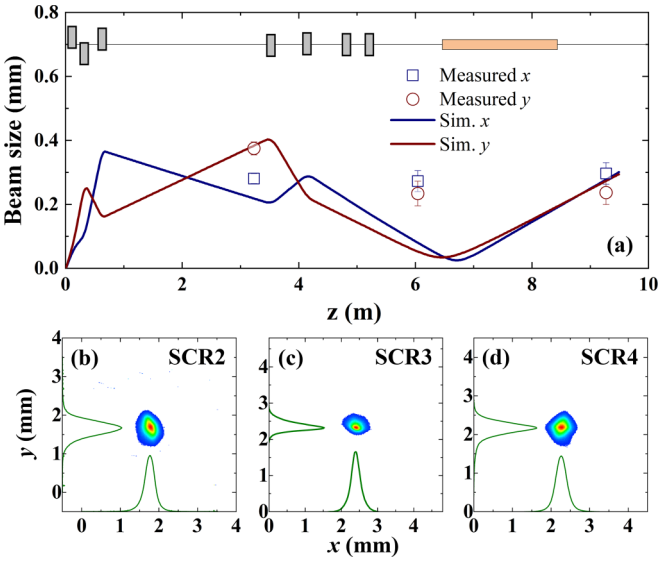


FIG. 10. Measured (blue and red dots) and GPT-simulated (blue and red solid lines) electron-beam envelope along the beamline. The polarities and strengths of the quadrupole magnets are indicated by the gray boxes at the top. The position of the undulator is marked by the orange box.

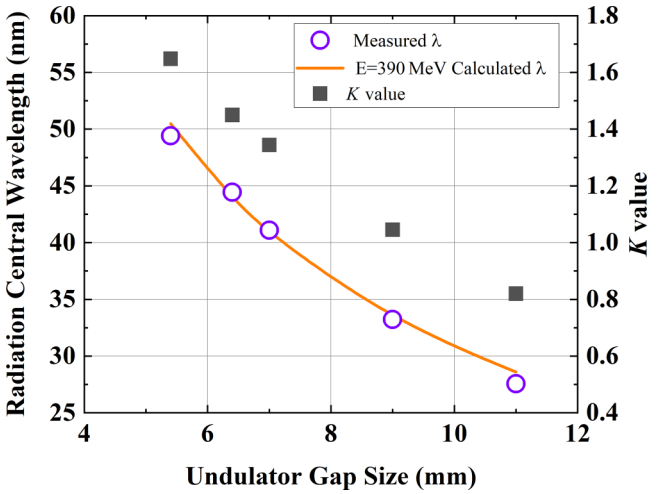


FIG. 11. The resonant wavelength and K value of the undulator vs the gap size. The black squares and purple circles represent the measured K value and radiation wavelength, respectively, as functions of the gap size. The orange solid line shows the calculated undulator radiation wavelength assuming an electron-beam energy of 390 MeV.

IX. BEAM TRANSPORTATION

The electron beams were transported through a beamline with a total length of approximately 9 m, as shown in Fig. 1. A permanent magnetic quadrupole (PMQ) triplet was positioned immediately after the beam exits the plasma, with its entrance located 110 mm from the electron source. Further focusing was achieved using four electromagnetic quadrupoles (EMQs 1–4), which guided the beam into the undulator.

Three removable phosphor screens (DRZ-Fine, SCR 2–4) are installed at strategic locations: before EMQ 1, at the undulator entrance, and after the undulator exit, respectively. Beam axis fine-tuning was facilitated by two two-axis steering magnets. Additionally, two current monitors (CT 1 and CT 2), placed before and after the beamline, confirm negligible charge loss during transportation.

The measured electron-beam sizes in horizontal (vertical) directions at SCR 2, SCR 3, and SCR 4 were 0.281 ± 0.016 mm (0.375 ± 0.020 mm), 0.273 ± 0.033 mm (0.234 ± 0.038 mm), and 0.297 ± 0.033 mm (0.237 ± 0.037 mm), respectively, are shown in Fig. 10. The results show reasonable agreement with GPT simulations, although some discrepancies remain, likely due to shot-to-shot electron beam instability in the experiments.

Since ESM 1 was excluded from the beamline, a second electron spectrometer (ESM 2) is positioned after the undulator. This spectrometer bent the electron beam into a beam damper and measured the beam energy.

X. UNDULATOR

The undulator strength parameter can be given by $K = eB\lambda_u/(2\pi m_e c)$, where e is the electron charge, B is the magnetic field, λ_u is the spatial period of the undulator magnets, m_e is the electron rest mass, and c is the speed of light.

We have installed a 2-m-long, variable-strength undulator composed of permanent magnets with a period of $\lambda_u = 25$ mm (80 periods in total). The undulator consists of two 1-m-long modules, each capable of independently adjusting its magnetic gap. To counteract the strong attractive force between opposing magnet rows, two additional surrounding rows of magnets are employed [34]. This configuration significantly reduces the mechanical load, resulting in a lightweight structure—approximately 500 kg per module—compared to conventional in-vacuum undulators. A photograph of the undulator is shown in Fig. 15.

The magnetic field strength of the undulator (K value) is tunable via adjustment of the gap size. The dependence of the measured K value on gap size is shown by the black squares in Fig. 11. In our experiments, the gap size was varied from 30 to 6.4 mm, corresponding to a tunable K value range of 0–1.45.

XI. AMPLIFIED UNDULATOR RADIATION

The radiation generated while the electron beam passes through the undulator has a central wavelength $\lambda_r = (1 + K^2/2)2\gamma^2$, which is in XUV range with our parameters. Details of the XUV detectors can be found in the Appendix. The purple circles in Fig. 11 are the measured undulator wavelengths with different gap sizes (i.e., K values). The results show good agreement with the calculation (orange curve) with a 390 MeV electron-beam energy.

The dependence of the measured XUV radiation intensity on the undulator K value is shown as green rectangles in Fig. 12. For low K values, a linear relationship is observed, consistent with the calculated spontaneous emission curve. In contrast, for $K > 0.4$, the radiation intensity increases more rapidly, suggesting the onset of nonlinear gain.

To reproduce the experimental measurements, we employed the SIMPLEX code to simulate the undulator radiation, using electron-beam parameters obtained from GPT

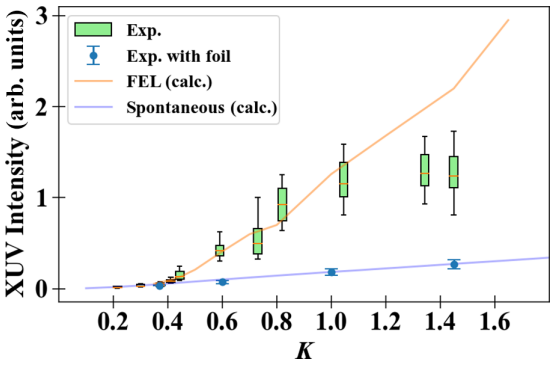


FIG. 12. Measured XUV radiation intensity with gain (green rectangles) and without gain (spontaneous emission, blue dots). The blue solid line represents the calculated spontaneous emission curve, while the orange line shows simulation results obtained using the SIMPLEX code.

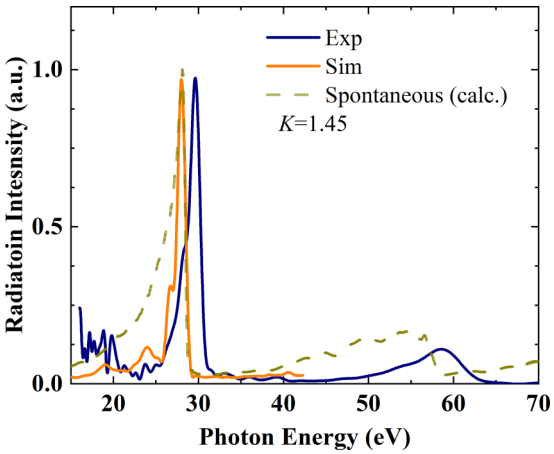


FIG. 13. The radiation spectrum at an undulator K value of 1.45, obtained from experimental measurements and SIMPLEX simulations, is shown as blue and orange solid lines, respectively. The yellow dashed line represents the calculated spectrum using the SPECTRA code.

simulations, which were based on input from PIC simulations. The simulated radiation intensity (orange solid line) shows good agreement with the experimental data. However, for K values greater than 1, the measured intensities are lower than the numerical predictions. This discrepancy may be attributed to the reduced undulator gap required for higher K values, which increases sensitivity to misalignment. In such cases, precise coaxial alignment between the electron beam and the undulator becomes critical. The limited pointing stability of our LWFA-generated electron beam poses a challenge for achieving optimal alignment, potentially leading to reduced XUV radiation yield.

It should be noted that minor adjustments to the input parameters were necessary to reproduce the FEL gain. Specifically, the electron-beam energy spread was reduced from 0.8% to 0.5%. This parameter modification may be attributed to slight discrepancies between the PIC simulation results and actual experimental conditions. Although the simulations predicted a minimum achievable energy spread of approximately 0.8%, experimental measurements suggested that narrower spreads (approximately 0.2%–0.7%, as discussed in Sec. VII) were attainable.

For further evidence, a 1.5-μm-thickness aluminum foil was installed before the undulator entrance to degrade the electron-beam emittance, to eliminate the self-amplification gain. The emittance growth factor is ∼200 due to multiple scattering of the electron beam in the foil. As predicted, the measured XUV radiation intensity well follows the linear relationship with the K value, shown as the blue dots in Fig. 12. It is also worth noting that, in cases exhibiting gain, the radiation intensity fluctuations are significantly larger compared to those observed in spontaneous emission. This behavior further indicates the presence of nonlinear gain.

The blue solid line in Fig. 13 shows the measured radiation spectrum at a K value of 1.45, while the orange solid line represents the result from SIMPLEX simulations. A peak photon energy mismatch of approximately 1 eV is observed, which can be attributed to fluctuations in the LWFA electron-beam energy. Despite this offset, the overall spectral shape shows good agreement. The yellow dashed line corresponds to the calculated spontaneous emission spectrum obtained using the SPECTRA code [35,36]. A distinct broadening tail is observed on the low-energy side. The clear difference between the measured/simulated spectrum and the spontaneous spectrum provides further evidence of nonlinear gain.

XII. CONCLUSIONS

We have presented a proof-of-concept demonstration of LWFA-based FEL amplification in the XUV range. Significant efforts to improve both laser and gas flow stability have led to marked enhancements in electron-beam quality. In addition, fine control of beam loading and phase rotation enabled the generation of monoenergetic electron beams with narrow energy spread and high peak energy density. By focusing the beam into a 2-m-long undulator, we observed exponential energy gain of the emitted undulator radiation, consistent with FEL amplification.

It should be noted, however, that the amplification remains subject to fluctuations, highlighting the need for further improvements in LWFA stability, particularly in laser quality. Nevertheless, these results underscore the potential of developing a compact, low-cost FEL platform capable of delivering femtosecond-scale temporal resolution.

ACKNOWLEDGMENTS

This work was supported by the JST-MIRAI Program (Grant No. JPMJMI17A1). We acknowledge SMARTSHELL Co., Ltd. for valuable discussions and technical assistance. Additionally, we extend our sincere gratitude to Prof. Y. Sano, Program Manager of the JST-MIRAI Program; Prof. R. Kodama from the Institute of Laser Engineering (ILE) at the University of Osaka; Dr. T. Ishikawa, Director of the RIKEN SPring-8 Center; and Dr. T. Otsuka from Utsunomiya University for their substantial contributions to establishing the LAPLACIAN facility under the ImPACT program of the Council for Science, Technology, and Innovation, Cabinet Office, Government of

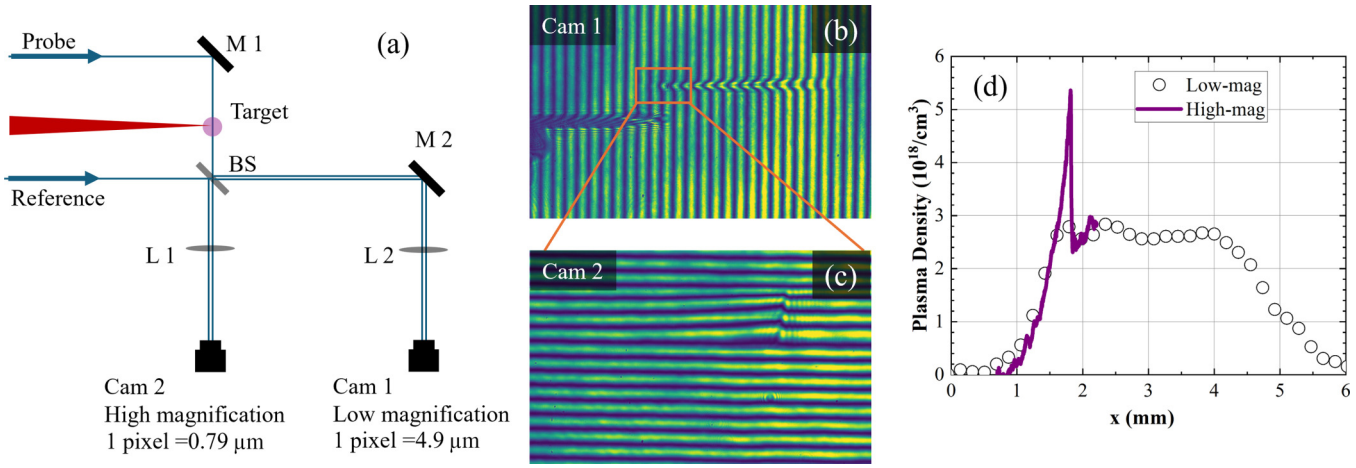


FIG. 14. Setup of a dual magnification Mach-Zehnder interferometer.

Japan. One of the authors (M.K.) acknowledges Dr. M. Ishino, Dr. T.-H. Dinh, Prof. Higashiguchi, Mr. R. Kurihara, Mr. Y. Koyanagi, and Mr. R. Soramoto for measuring the Al filter transmissivity using BL11D at KEK-PF (No. 2021G525).

DATA AVAILABILITY

The data that support the findings of this article are not publicly available. The data are available from the authors upon reasonable request.

APPENDIX

1. Plasma-density distribution

As shown in Fig. 14(a), in a Mach-Zehnder interferometer, a fringe phase shift is observed due to differences in refractivity along the two optical paths. Using Abel inversion, the plasma density can be estimated.

The plasma channel generated by a large f-number focusing laser typically has a long longitudinal length (in the order of millimeters) and a small transverse size (less than 0.1 mm). Consequently, interferometry fringes are often oriented vertically to achieve better spatial resolution along the transverse axis of the channel. However, this configuration compromises longitudinal resolution to improve the accuracy of phase-shift measurements. This trade-off becomes particularly problematic in shock injection experiments, where the shock wave thickness can be less than 10 μm.

Figure 14(b) provides an example image obtained from Camera 1, where the imaging system offers a pixel resolution of 4.9 μm and an optical resolution of 16 μm. Due to the fringe size, however, the longitudinal spatial resolution is restricted to approximately 470 μm, insufficient to resolve the fine details of the shock density. An additional isolated fringe appears at the shock position, but it is not possible to determine the accurate shock density with this configuration.

To address this issue, a second camera (Camera 2) with greater magnification was introduced. Additionally, a motorized beam splitter holder was used to align the fringes horizontally, improving longitudinal resolution. This setup achieves a pixel resolution of 0.79 μm and an optical resolution of 6 μm with a longitudinal field of view of approximately 1.5 mm. As shown in Fig. 14(b), the longitudinal distribution of the phase shift at the shock position can now be clearly resolved. However, the horizontal fringe orientation compromises spatial resolution in the transverse axis, making it difficult to determine the exact phase shift and, consequently, the absolute plasma density at the channel's center. Nevertheless, the relative density values before and after the shock remain reliable.

To reconstruct the full plasma-density distribution along the channel's center, the density measurements from Camera 2 were scaled to match the data from Camera 1, as shown in Fig. 14(d). The combined measurements provide a complete reconstruction of the plasma-density distribution along the entire channel. It should be noted that the stability of the gas jet is critical for this approach, as the data from Cameras 1 and 2 are not obtained from the same shot.

2. Estimation of energy spread

As described in Sec. II, our ESM consists of a dipole magnet with a field strength of 0.55 T. The electron beam enters the ESM, is bent by the Lorentz force, and is detected on a phosphor screen (DRZ-High). Two major effects contribute to an increase in the measured energy spread.

The first contribution is the finite transverse beam size. Because our mean beam size is small and the pointing stability is not yet sufficient to allow the use of an entrance slit, the transverse beam size broadens the measured energy distribution. The beam size s_e is estimated from the vertical beam size on the ESM screen, assuming that the transverse dimensions are identical.

The second contribution arises from the oblique incidence angle θ_i on the phosphor screen. The DRZ-High screen has a phosphor layer of thickness $d = 310$ μm. Oblique incidence increases the effective size of the fluorescence source and thus broadens the measured energy spread.

Assuming that the beam has a Gaussian-like distribution, the intrinsic energy spread can be estimated by deconvolving these contributions:

$$\Delta E_{\text{estimated}} = \sqrt{\Delta E_{\text{measured}}{}^2 - s_e{}^2 - (d \times \cos\theta_i)^2}.$$



FIG. 15. Photograph of the undulator assembly.

3. Undulator

The undulator used in the present investigation was constructed on the basis of a very short-period undulator technology using the plate monolithic magnet (PMM). We developed a multipole magnetization method to transcribe a very short-period undulator magnetic field onto a plate magnet [37]. This aims at shortening the period length of the undulator from a few tens of mm to about one-tenth of the usual length [37]. We established magnetization technology for PMMs with period length of a few mm and a connection method for lengthening the undulator magnet array [38]. Light source characterization experiment was performed successfully by using PMMs with 4-mm period length in a 35 MeV S-band linac [39]. A field strength of 3 kG is successfully obtained at a gap of 1.6 mm.

The PMM method is very useful to cancel magnetic attractive force acting between the undulator main row magnets. The undulator developed here has three magnet rows of PMMs on the upper and lower sides. Cancellation of the attractive force between the opposing main row PMMs is effectively made by additional repulsive PMMs surrounding the main rows [34].

Although the force cancellation method using the PMMs is developed originally for the very-short-period undulator, we find that it is also effective to the undulator magnet of ordinary period length. In the present investigation, we adopt a period length of $\lambda_u = 25$ mm as a light source of XUV undulator radiation. The undulator consists of two 1-m-long modules, each (40 periods) capable of independently adjusting its magnet gap. The above cancellation method is able to remove the mechanical load in driving axes of the undulator frame to almost a zero level, and to realize high-precision gap drive with a compact and light undulator frame (some 500 kg per module) [34]. A photograph of the undulator is shown in Fig. 15.

4. XUV detector

The XUV detector system is illustrated in Fig. 16. The imaging setup employs a grazing-incidence ellipsoidal mirror with a focal length of 1 m and an incidence angle of 86°. The ellipsoidal mirror has dimensions of 300 mm × 50 mm × 50 mm with a surface figure of $\lambda/95$ rms and $\lambda/13$ PV ($\lambda = 633$ nm). The object plane is positioned 1 m downstream of the undulator exit, and an x-ray CMOS camera (ANDOR, Marana-4BN6U-SOI) is placed at the image plane. Thin aluminum filters (100 or 800 nm) are used to block residual laser light.

In this configuration, the spatial profile of the undulator radiation can be recorded. For spectral measurements, a 2000 lines/mm transmission grating (NTT-AT) and a rectangular slit are inserted 40 mm in front of the camera sensor. The spectrometer achieves a resolution of approximately 0.1 eV at a photon energy of 20 eV with a slit width of 50 μm. The spectral resolution degrades at higher photon energy.

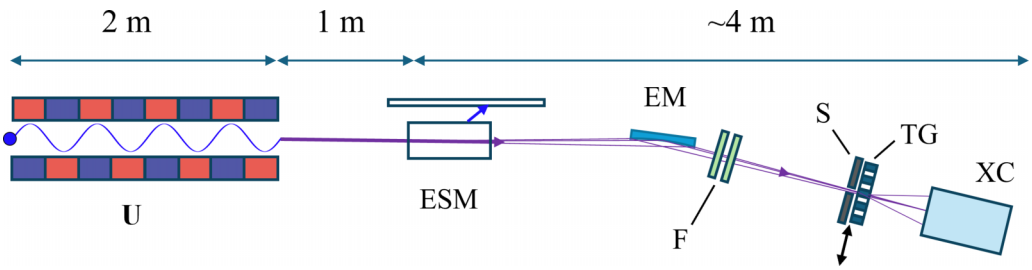


FIG. 16. Schematic of the XUV detector setup. U: undulator; ESM: electron spectrometer; EM: ellipsoidal mirror; F: optical blocking filters; S: slit; TG: transmission grating; XC: x-ray CMOS camera. The configuration shown corresponds to the spectrum measurement mode. For spatial distribution measurements, the slit and transmission grating are removed.

In order to estimate the photon numbers from the measured intensity, we used the following throughputs as follows. The mirror reflectivity is given by the manufacturer. The filter transmissivities are characterized at the synchrotron radiation facility (KEK-PF), the diffraction efficiency of the transmission grating is calculated with a numerical code. The sensitivity of the CMOS detector is used with nominal value given by the manufacturer.

[1] T. Tajima and J. M. Dawson, Laser electron-accelerator, Phys. Rev. Lett. **43**, 267 (1979).

[2] D. Strickland and G. Mourou, Compression of amplified chirped optical pulses, Opt. Commun. **56**, 219 (1985).

[3] W. P. Leemans, B. Nagler, A. J. Gonsalves, Cs. Tóth, K. Nakamura, C. G. R. Geddes, E. Esarey, C. B. Schroeder, and S. M. Hooker, GeV electron beams from a centimetre-scale accelerator, Nat. Phys. **2**, 696 (2006).

[4] W. P. Leemans, A. J. Gonsalves, H.-S. Mao, K. Nakamura, C. Benedetti, C. B. Schroeder, Cs. Tóth, J. Daniels, D. E. Mittelberger, S. S. Bulanov, J.-L. Vay, C. G. R. Geddes, and E. Esarey, Multi-GeV electron beams from capillary-discharge-guided subpetawatt laser pulses in the self-trapping regime, Phys. Rev. Lett. **113**, 245002 (2014).

[5] A. J. Gonsalves, *et al.*, Petawatt laser guiding and electron beam acceleration to 8 GeV in a laser-heated capillary discharge waveguide, Phys. Rev. Lett. **122**, 084801 (2019).

[6] A. R. Maier, N. Delbos, T. Eichner, L. Hubner, S. Jalas, L. Jeppe, S. W. Jolly, M. Kirchen, V. Leroux, P. Messner, M. Schnepp, M. Trunk, P. A. Walker, C. Werle, and P. Winkler, Decoding sources of energy variability in a laser-plasma accelerator, Phys. Rev. X **10**, 031039 (2020).

[7] C. Emma, *et al.*, Free electron lasers driven by plasma accelerators: Status and near-term prospects, High Power Laser Sci. Eng. **9**, e57 (2021).

[8] W. Wang, *et al.*, Free-electron lasing at 27 nanometres based on a laser wakefield accelerator, Nature (London) **595**, 516 (2021).

[9] M. Labat, *et al.*, Seeded free-electron laser driven by a compact laser plasma accelerator, Nat. Photon. **17**, 150 (2023).

[10] S. K. Barber, *et al.*, Greater than 1000-fold gain in a free-electron laser driven by a laser-plasma accelerator with high reliability, Phys. Rev. Lett. **135**, 055001 (2025).

[11] T. André, *et al.*, Control of laser plasma accelerated electrons for light sources, Nat. Commun. **9**, 1334 (2018).

[12] A. Pukhov and J. Meyer-ter-vehn, Laser wake field acceleration: The highly non-linear broken-wave regime, Appl. Phys. B **74**, 355 (2002).

[13] Z.-M. Sheng, M. Chen, Y.-Y. Ma, and J. Zhang, Theory of ionization-induced trapping in laser-plasma accelerators, J. Appl. Phys. **99**, 056109 (2006).

[14] A. Pak, K. A. Marsh, S. F. Martins, W. Lu, W. B. Mori, and C. Joshi, Injection and trapping of tunnel-ionized electrons into laser-produced wakes, Phys. Rev. Lett. **104**, 025003 (2010).

[15] R. Lehe, A. F. Lifschitz, X. Davoine, C. Thaury, and V. Malka, Optical transverse injection in laser-plasma acceleration, Phys. Rev. Lett. **111**, 085005 (2013).

[16] A. Buck, J. Wenz, J. Xu, K. Khrennikov, K. Schmid, M. Heigoldt, J. M. Mikhailova, M. Geissler, B. Shen, F. Krausz, S. Karsch, and L. Veisz, Shock-front injector for high-quality laser-plasma acceleration, Phys. Rev. Lett. **110**, 185006 (2013).

[17] M. Kirchen, S. Jalas, P. Messner, P. Winkler, T. Eichner, L. Hübner, T. Hülsenbusch, L. Jeppe, T. Parikh, M. Schnepp, and A. R. Maier, Optimal beam loading in a laser-plasma accelerator, Phys. Rev. Lett. **126**, 174801 (2021).

[18] J. Götzfried, A. Döpp, M. F. Gilljohann, F. M. Foerster, H. Ding, S. Schindler, G. Schilling, A. Buck, L. Veisz, and S. Karsch, Physics of high-charge electron beams in laser-plasma wakefields, Phys. Rev. X **10**, 041015 (2020).

[19] N. Nakanii, K. Huang, K. Kondo, H. Kiriyama, and M. Kando, Precise pointing control of high-energy electron beam from laser wakefield acceleration using an aperture, Appl. Phys. Express **16**, 026001 (2023).

[20] C. Zhu, J. Wang, Y. Li, J. Feng, D. Li, Y. He, J. Tan, J. Ma, X. Lu, Y. Li, and L. Chen, Optical steering of electron beam in laser plasma accelerators, Opt. Express **28**, 11609 (2020).

[21] Z. Lei, Y. Gu, Z. Jin, S. Sato, A. Zhidkov, A. Rondepierre, K. Huang, N. Nakanii, I. Daito, M. Kando, and T. Hosokai, Supersonic gas jet stabilization in laser–plasma acceleration, High Power Laser Sci. Eng. **11**, e91 (2023).

[22] Z. Lei, Z. Jin, Y. Gu, S. Sato, A. Zhidkov, A. Rondepierre, K. Huang, N. Nakanii, I. Daito, M. Kando, and T. Hosokai, Modular supersonic nozzle for the stable laser-driven electron acceleration, Rev. Sci. Instrum. **95**, 015111 (2024).

[23] Y. Gu, Z. Jin, Z. Lei, S. Sato, K. Huang, N. Nakanii, I. Daito, M. Kando, and T. Hosokai, Generation of highly stable electron beam via the control of hydrodynamic instability, Sci. Rep. **14**, 31162 (2024).

[24] G. G. Manahan, A. F. Habib, P. Scherkl, P. Delinikolas, A. Beaton, A. Knetsch, O. Karger, G. Wittig, T. Heinemann, Z. M. Sheng, J. R. Cary, D. L. Bruhwiler, J. B. Rosenzweig, and B. Hidding, Single-stage plasma-based correlated energy spread compensation for ultrahigh 6D brightness electron beams, Nat. Commun. **8**, 15705 (2017).

[25] R. Lehe, M. Kirchen, I. A. Andriyash, B. B. Godfrey, and J.-L. Vay, A spectral, quasi-cylindrical and dispersionfree particle-in-cell algorithm, Comput. Phys. Commun. **203**, 66 (2016).

[26] S. Y. Kalmykov, S. A. Yi, A. Beck, A. F. Lifschitz, X. Davoine, E. Lefebvre, V. Khudik, G. Shvets, and M. C. Downer, Dark-current-free petawatt laser-driven wakefield accelerator based on electron self-injection into an expanding plasma bubble, Plasma Phys. Controlled Fusion **53**, 014006 (2011).

[27] A. Döpp, C. Thaury, E. Guillaume, F. Massimo, A. Lifschitz, I. Andriyash, J.-P. Goddet, A. Tazfi, K. Ta Phuoc, and V. Malka, Energy-chirp compensation in a laser wakefield accelerator, Phys. Rev. Lett. **121**, 074802 (2018).

[28] L. Ke, C. Yu, K. Feng, Z. Qin, K. Jiang, H. Wang, S. Luan, X. Yang, Y. Xu, Y. Leng, W. Wang, J. Liu, and R. Li, Optimization of electron beams based on plasma-density modulation in a laser-driven wakefield accelerator, Appl. Sci. **11**, 2560 (2021).

[29] H.-E. Tsai, K. K. Swanson, S. K. Barber, R. Lehe, H.-S. Mao, D. E. Mittelberger, S. Steinke, K. Nakamura, J. van Tilborg, C. Schroeder, E. Esarey, C. G. R. Geddes, and W. Leemans,

Control of quasi-monoenergetic electron beams from laser-plasma accelerators with adjustable shock density profile, Phys. Plasmas **25**, 043107 (2018).

[30] F. Irshad, S. Karsch, and A. Döpp, Multi-objective and multi-fidelity Bayesian optimization of laser-plasma acceleration, Phys. Rev. Res. **5**, 013063 (2023).

[31] Pulsar Physics, General Particle Tracer, www.pulsar.nl/gpt.

[32] T. Tanaka, simplex: Simulator and postprocessor for free-electron laser experiments, J. Synchrotron Radiat. **22**, 1319 (2015).

[33] T. Tanaka, Accelerating the convergence of free electron laser simulations by retrieving a spatially coherent component of microbunching, Phys. Rev. Accel. Beams **27**, 030703 (2024).

[34] S. Yamamoto, Undulator light source with a compact slender and light frame based on a magnet technology developed for very-short-period undulators, J. Phys.: Conf. Ser. **3010**, 012028 (2025).

[35] T. Tanaka and H. Kitamura, SPECTRA: A synchrotron radiation calculation code, J. Synchrotron Radiat. **8**, 1221 (2001).

[36] T. Tanaka, Major upgrade of the synchrotron radiation calculation code SPECTRA, J. Synchrotron Radiat. **28**, 1267 (2021).

[37] S. Yamamoto, A novel attempt to develop very short period undulators, J. Phys.: Conf. Ser. **425**, 032014 (2013).

[38] S. Yamamoto, Development of very short period undulators, in *Proc. IPAC18, Vancouver, BC, Canada, WEXGBD1* (2018), p. 1735.

[39] S. Yamamoto, S. Kashiwagi, S. Masuda, N. Nakanii, T. Hosokai, M. Kando, T. Muto, K. Nanbu, F. Hinode, and H. Hama, Light source based on a 100 mm-long monolithic undulator magnet with a very short 4 mm-period length, J. Synchrotron Radiat. **26**, 1902 (2019).